Journal of Materials Research and Technology 42 (2026) 6742–6755

Contents lists available at ScienceDirect

Journal of Materials Research and Technology

journal homepage: www.elsevier.com/locate/jmrt

Annealing-induced hardening in an ultrafine-grained Mg–Zn–Ca alloy processed by high pressure torsion

N. Mirabdolazimi [a], M. Reihanian [b], E. Bagherpour [c], C.L. Mendis [c], A. Rezvani [a], R.Z. Valiev [d], R. Ebrahimi [a,*]

[a] Department of Materials Science and Engineering, School of Engineering, Shiraz University, Shiraz, Iran
[b] Department of Materials Science and Engineering, Faculty of Engineering, Shahid Chamran University of Ahvaz, Ahvaz, Iran
[c] Brunel Centre for Advanced Solidification Technology (BCAST), Brunel University of London, Uxbridge, UB8 3PH, UK
[d] Institute of Physics of Advanced Materials, Ufa University of Science and Technology, Ufa, 450076, Russia

ARTICLE INFO

Keywords:
Magnesium alloy
High-pressure torsion (HPT)
Annealing-induced hardening
Microstructure
Ultrafine-grained microstructure
Microhardness

ABSTRACT

The microstructural evolution and hardness behavior of an Mg–1Zn–0.2Ca alloy processed by high-pressure torsion (HPT) and subsequent annealing were systematically investigated. The initial grain size of ~105 μm was refined to the ultrafine regime after HPT processing and subsequent annealing, with average grain sizes of 1.62–1.97 μm depending on annealing time. Post-deformation annealing at 300–400 °C revealed an unusual non-monotonic hardness response characterized by an initial decrease followed by a pronounced increase with increasing annealing time. Quantitative optical microscopy confirmed progressive grain coarsening during annealing, indicating that the secondary hardening cannot be attributed to further grain refinement. Electron backscatter diffraction (EBSD) analysis revealed a reduction in local misorientation and grain orientation spread at intermediate annealing times, indicating heterogeneous recovery rate within the ultrafine-grained structure. With increasing annealing time, a decrease in basal texture intensity was observed, accompanied by crystallographic reorientation. These microstructural and textural changes modify the deformation geometry under indentation and are responsible for the abnormal hardness increase observed during annealing. These findings highlight the critical role of microstructural recovery and crystallographic orientation in governing the post-annealing mechanical response of HPT-processed Mg alloys.

1. Introduction

Magnesium (Mg) alloys have attracted significant attention in various engineering applications due to their low density, high specific strength, and excellent biocompatibility [1]. Among these, Mg–Zn–Ca alloys stand out as promising materials due to their favorable combination of mechanical properties, corrosion resistance, and biocompatibility [2]. Zinc (Zn) refines the grain structure and enhances strength, while calcium (Ca) improves biodegradability [3]. However, despite these advantages, refining the grain structure of Mg–Zn–Ca alloys and enhancing their performance in biological applications requires advanced processing techniques to improve their structural integrity and functional capabilities.

Severe plastic deformation (SPD) techniques have been widely employed to enhance the mechanical properties of Mg alloys by introducing ultrafine-grained (UFG) microstructures [4,5] for biomedical applications [6]. Since Mg alloys are difficult to deform, the SPD processing of these alloys is carried out at temperatures higher than room temperature [7–9]. However, the effectiveness of SPD at high temperatures is often constrained by grain growth and dynamic recrystallization. Therefore, it is desirable to process Mg alloys via SPD at lower temperatures. High-pressure torsion (HPT) is a promising SPD technique that enables grain refinement and improved mechanical properties by applying high pressure and shear deformation between rotating anvils [10,11]. Since its first application to Mg alloys in the early 1990s [12,13], HPT has been extensively studied for processing various Mg-based alloys, including Mg–Zn–Ca systems.

Several studies have explored the impact of HPT on the microstructure, mechanical properties and particularly corrosion behavior of Mg–Zn–Ca alloys. Zhang et al. [14] revealed that after five revolutions of HPT, the grain size was significantly refined to 130–150 nm, and the second phases were uniformly distributed. This structural refinement led

* Corresponding author.
E-mail address: ebrahimy@shirazu.ac.ir (R. Ebrahimi).

https://doi.org/10.1016/j.jmrt.2026.04.245
Received 10 April 2026; Received in revised form 25 April 2026; Accepted 27 April 2026
Available online 30 April 2026

to a more homogeneous corrosion process, where the entire alloy surface corroded at a nearly uniform rate. Gao et al. [15] demonstrated that HPT processing resulted in the transformation of the second-phase particles into nanoscale features, which were uniformly dispersed within the grain interiors rather than accumulating along grain boundaries. As a result, the corrosion behavior of the HPT-treated sample was more homogeneous compared to its as-cast counterpart. Further research by Zhang et al. [16] indicated that in solution-treated Mg–Zn–Ca alloys, the second-phase particles dispersed more uniformly after HPT, whereas in cast alloys without prior solution treatment, the second phases remained incompletely fragmented and exhibited non-uniform distribution. The microhardness of the HPT-processed solution-treated alloy was significantly improved, with a more homogeneous hardness distribution. Moreover, the corrosion resistance of the solution treated alloy was superior to that of the cast alloy in physiological environments. Guan et al. [17] reported that the HPT processed Mg–Zn–Ca alloy exhibited enhanced degradation properties and superior microhardness compared to as-cast Mg alloy. Medeiros et al. [18] indicated that while HPT processing generally improved strength, deformation localization could occur in Mg–Zn–Ca and Mg–Y–RE alloys. Brunner et al. [19] showed that HPT-induced deformation significantly reduced corrosion resistance. Kulyasova et al. [20] demonstrated that although HPT processing resulted in substantial grain refinement—down to 210 nm for Mg–1Ca and 90 nm for Mg–1Zn-0.2Ca—the corrosion resistance varied considerably, differing by an order of magnitude.

Despite the mentioned research on the HPT processing of Mg–Zn–Ca alloys, studies on the effects of subsequent annealing after HPT remain limited, and the existing results are often contradictory. Zhang et al. [21] focused on grain size evolution and corrosion behavior of HPT-processed Mg–Zn–Ca in simulated body fluid, with minimal discussion of mechanical properties, except for surface stress, which initially decreased and then increased upon annealing. In a separate study, Zhang et al. [22] revealed a significant increase in microhardness following HPT, with higher values concentrated at the edges of the sample. However, annealing resulted in a reduction in microhardness, accompanied by a more uniform hardness distribution across the material. Kulyasova et al. [23] reported a remarkable increase in microhardness of an HPT-processed Mg–Zn–Ca alloy (up to 990 MPa) due to the formation of an UFG microstructure (~150 nm grain size). After annealing at 200 °C, the alloy exhibited an ultimate tensile strength of 270 MPa with a ductility of 9%. In contrast, Horky et al. [24] processed two biodegradable Mg–Zn–Ca alloys via HPT followed by annealing. Surprisingly, annealing at approximately $0.45T_m$ resulted in further enhancements to hardness and tensile strength, surpassing even the improvements gained solely from HPT. This unexpected strengthening was attributed to vacancy agglomeration and dislocation loop formation within the basal plane, effectively impeding dislocation motion.

Although annealing-induced hardening (AH) has been reported in several severely deformed materials, its underlying mechanisms in HPT-processed Mg–Zn–Ca alloys remain insufficiently understood. Most existing studies focus primarily on grain refinement effects or general recovery behavior, while detailed correlations between hardness evolution and EBSD-based parameters such as GOS, KAM, misorientation distribution, and texture evolution during short-term annealing are limited. Therefore, the present study aims to investigate the microstructural and crystallographic evolution of an Mg–1Zn–0.2Ca alloy processed by HPT and subsequently annealed at different temperatures and times, with particular emphasis on elucidating the mechanisms responsible for the observed abnormal hardness variation. By integrating quantitative optical analysis with comprehensive EBSD characterization, this work provides new insight into the interplay between recovery, texture evolution, and mechanical response in severely deformed Mg alloys, contributing to a deeper understanding of strength tailoring through post-deformation heat treatment.

2. Materials and method

The initial material used in this study was an as-cast Mg–1Zn-0.2Ca alloy. The chemical composition of the alloy is presented in Table 1. The HPT specimens were in the form of discs with a diameter of 15 mm and a thickness of 3 mm prior to processing. HPT processing was employed to induce severe plastic deformation. The alloy was subjected to HPT at room temperature for 0.5, 1, 2, and 3 rotations under an applied pressure of 1.2 GPa [25]. To calculate the effective strain, the strains induced by the two deformation stages must be determined separately and then combined. The effective strain resulting from the first stage ($\bar{\varepsilon}_1$) is calculated using Eq. (1), similar to the case of uniaxial compression testing. This strain is approximately uniform throughout the specimen:

$$\bar{\varepsilon}_1 = \ln\frac{H_\circ}{H} \tag{1}$$

where $H_\circ$ is the initial thickness of the specimen and H is the thickness after compression. The shear strain (γ) induced by the torsion stage is determined using Eq. (2):

$$\gamma = \frac{2\pi Nr}{H} \tag{2}$$

where N is the number of revolutions applied during torsion, and r is the radial distance from the center of the disk. For shear strains $\gamma > 0.8$, the effective strain contributed by the torsion stage ($\bar{\varepsilon}_2$) is calculated by Eq. (3) [26]:

$$\bar{\varepsilon}_2 = \left[\frac{4}{3}\left[ln\sqrt{\gamma^2+1}\right]^2 + \frac{(tan^{-1}\,\gamma)^2}{3}\right]^{1/2} \tag{3}$$

The strain applied during the torsion stage is not uniformly distributed throughout the specimen; its magnitude increases with increasing distance from the center. The total effective strain imposed on the material is finally obtained by summing the contributions from both stages according to Eq. (4):

$$\bar{\varepsilon}_t = \bar{\varepsilon}_1 + \bar{\varepsilon}_2 \tag{4}$$

The sample processed for 1 rotation was selected as the typical sample for subsequent heat treatment studies. These samples were annealed at varying temperatures (300 to 400 ċ) and holding times (30 to 300 s) to investigate the thermal stability and microstructural evolution of the alloy. To preserve the microstructure, specimens were water-quenched immediately upon reaching the target conditions. To mitigate corrosion risks—arising from high applied strains and low alloy resistance—isothermal sand-embedding was employed. The sand and container were pre-heated to the target temperature prior to specimen immersion. Based on the lumped capacitance method [27], the specimens reached thermal equilibrium within milliseconds due to their small dimensions and high heat transfer coefficient, ensuring rapid and uniform heating.

The microstructural evolution of the HPT-processed and heat-treated samples was analyzed using optical microscopy. Samples for optical microscopy were prepared by standard metallographic techniques, including grinding, polishing, and etching. The polished samples were etched with Acetic Picral reagent (10 ml acetic acid, 4.2 g picric acid, 10 ml distilled water, 70 ml ethanol) for 5-10 s using an immersion method. Micrographs were taken at three different locations on the disc, at distances of 2 mm, 4 mm, and 6 mm from the center, to assess the microstructural homogeneity and variations across the sample.

A custom MATLAB code was developed to conduct comprehensive microstructural analysis in accordance with the ASTM E1382 standard. The original optical microscopy image was first preprocessed using commercial image processing software to enhance contrast and clarity, ensuring accurate feature detection. Subsequently, grain boundaries were traced and extracted to generate a binary representation of the

Table 1
Chemical composition of the Mg–1Zn-0.2Ca used in this study.

Element	Mg	Si	Zn	Al	Be	Ca	Fe	Pb
Weight (%)	98.60967	0.05	1.001	0.04	0.00123	0.212	0.003	0.0129

microstructure using MATLAB's Image Processing Toolbox. The custom-developed code facilitated precise grain identification, indexing, and quantification, enabling detailed characterization of morphological parameters such as grain size and distribution.

For EBSD analysis, the sectioned samples were first ground and mechanically polished, followed by electro-polishing in a 15% nitric acid + methanol solution at −25 °C for 60 s. This electro-polishing step effectively removed the surface deformation layer introduced during mechanical preparation. EBSD data were collected using a Zeiss Crossbeam 340 SEM–FIB system operated at an accelerating voltage of 20 kV. Orientation maps were acquired with a step size of 0.5 μm. EBSD patterns were indexed using EDAX TEAM™ software, and the resulting datasets were processed and analyzed with OIM Analysis™ version 8. All microstructural characterizations, including optical microscopy and EBSD analyses, were conducted on the side section of the HPT-processed discs. In view of the specific microstructural phenomena observed in the Mg–1Zn–0.2Ca alloy, the present study focused on spatially resolved crystallographic techniques (EBSD) to provide a statistically significant correlation between local misorientation and mechanical hardening. While supplemental surface-sensitive or macro-scale diffraction techniques are often employed in diverse material systems to elucidate molecular or chemical states [28–30], the high-resolution orientation mapping and local strain analysis used here were deemed sufficient to identify the primary metallurgical drivers-texture reorientation and recovery heterogeneity-responsible for the observed hardening.

Vickers hardness measurements were performed on the HPT-processed and heat-treated samples to evaluate their mechanical properties. Hardness tests were conducted using a Vickers hardness tester (KOOPA microhardness tester MH1) with an applied load of 200 g and a dwell time of 10 s. Hardness measurements were performed on the side section of the HPT-processed discs at radial distances ranging from 1 mm to 6 mm from the center, with an interval of 1 mm, in order to evaluate the variation in mechanical response as a function of imposed strain.

3. Results

3.1. Initial microstructure and hardness of the as-cast alloy

Fig. 1 shows the optical microstructure of the as-cast Mg–1Zn–0.2Ca alloy prior to HPT processing. The microstructure is characterized by coarse, equiaxed grains with an average grain size of approximately 105 μm, indicating a typical as-cast magnesium alloy structure formed under relatively low solidification rates. The presence of such large grains reflects the absence of any prior thermomechanical processing and serves as a baseline condition for evaluating the effects of severe plastic deformation. The corresponding average microhardness of 49.5 Hv is relatively low, which is consistent with the coarse-grained structure and the limited contribution of grain boundary strengthening in the as-cast state. At this stage, the mechanical response of the alloy is mainly governed by solid-solution strengthening from Zn and Ca and by the intrinsic properties of the Mg matrix. This initial microstructure highlights the significant potential for microstructural refinement and mechanical enhancement through subsequent HPT processing.

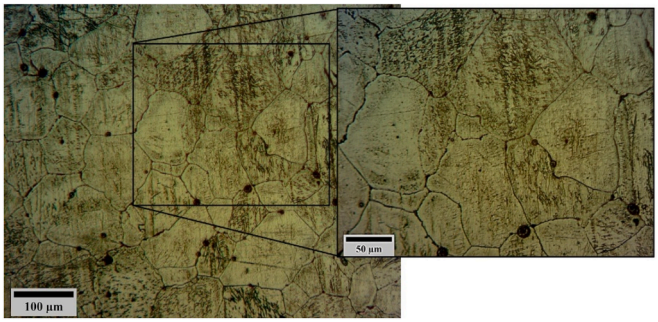

Fig. 1. Optical micrograph of the as-cast Mg–1Zn–0.2Ca alloy.

3.2. Microstructural evolution after HPT processing

Fig. 2 presents optical micrographs of the Mg–1Zn–0.2Ca alloy after HPT processing at different numbers of rotations and radial distances from the disc center, illustrating the overall microstructural evolution induced by severe plastic deformation. With increasing HPT rotations and increasing radial distance, the microstructure appears progressively more refined, reflecting the increase in imposed shear strain during HPT processing. However, due to the resolution limitations of optical microscopy at the selected magnification, the extent of grain refinement in heavily deformed regions is not clearly resolved in Fig. 2, particularly for samples subjected to higher rotations and located at larger radial distances. In these regions, the microstructure appears as a highly deformed and featureless contrast, which is commonly observed in UFG magnesium alloys processed by severe plastic deformation when examined at low to moderate magnifications. To clearly reveal and quantitatively assess the refined grain structure, a representative condition corresponding to 3 HPT turns at a radial distance of 6 mm-where the highest strain is imposed-was selected for detailed examination. A magnified view of this condition, along with traced and highlighted grain boundaries, is presented in Fig. 3. This approach allows the grain refinement induced by HPT processing to be clearly visualized and accurately quantified, overcoming the limitations observed in Fig. 2.

Fig. 3a shows a magnified optical micrograph of the alloy. The microstructure is characterized by a highly refined grain structure with grains that are predominantly elongated along the shear direction, which is a typical feature of severe plastic deformation by HPT. The inset with traced grain boundaries highlights the ultrafine nature of the grains and confirms the effectiveness of grain boundary delineation used for quantitative analysis. Despite the severe deformation, the grain structure appears relatively uniform, indicating that extensive grain subdivision and continuous dynamic recrystallization have occurred. The average grain size measured from this condition is approximately 1.5 μm, representing a drastic refinement compared to the as-cast state.

Fig. 3b shows the corresponding grain size frequency histogram obtained from image analysis of the microstructure shown in Fig. 3a. The distribution spans grain sizes primarily between ~0.5 and 3 μm, with a peak centered around ~1–2 μm, confirming the dominance of ultrafine grains. The slightly asymmetric tail toward larger grain sizes suggests the presence of a limited fraction of relatively coarser grains, which may be associated with incomplete recrystallization or local strain heterogeneities. Nevertheless, the narrow overall distribution indicates a high degree of microstructural uniformity at this radial position. The UFG structure and relatively uniform grain size distribution achieved after 3 HPT turns are consistent with the observed increase in microhardness to 91.6 Hv, which can be mainly attributed to grain boundary strengthening in accordance with the Hall–Petch relationship, along with the high dislocation density introduced during HPT processing.

Fig. 4 illustrates the variation in Vickers hardness of the Mg–1Zn–0.2Ca alloy as a function of distance from the disc center

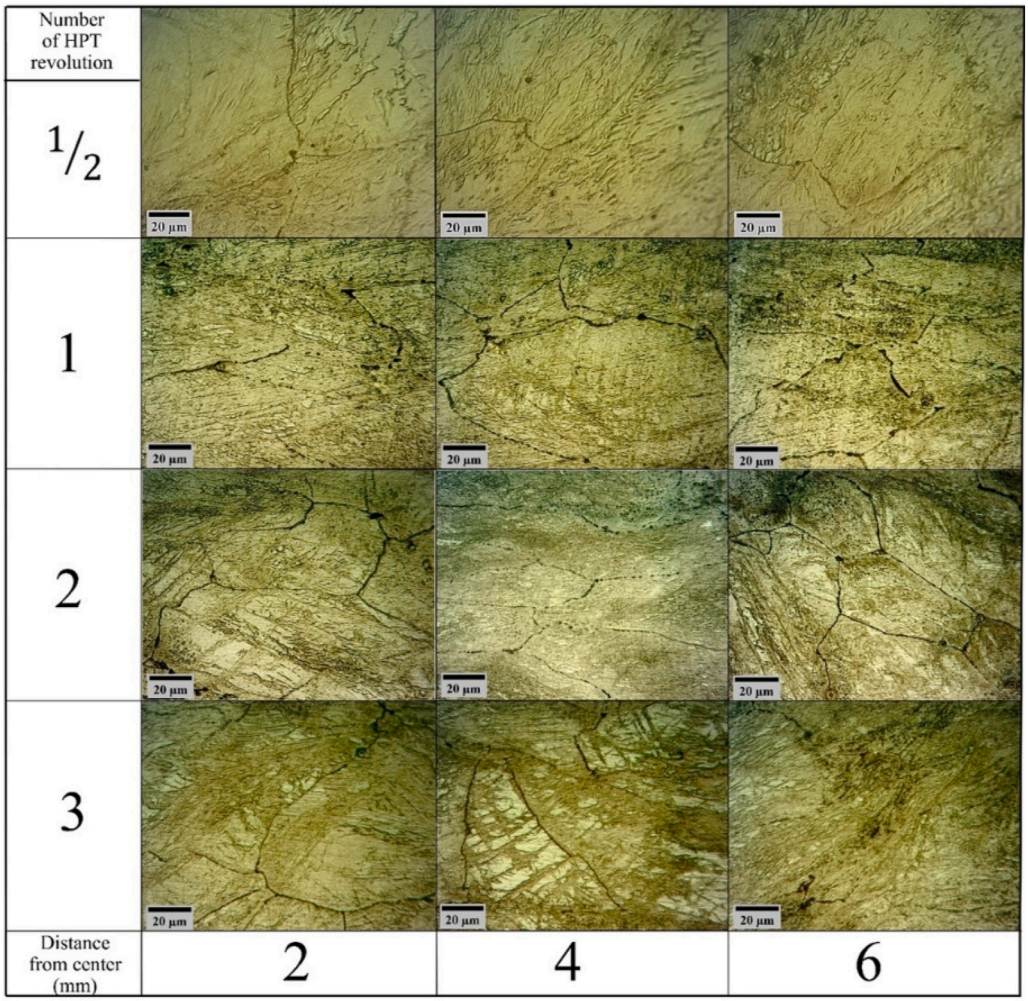

Fig. 2. Optical micrographs of the Mg–1Zn–0.2Ca alloy after HPT processing at different numbers of rotations and radial distances from the disc center.

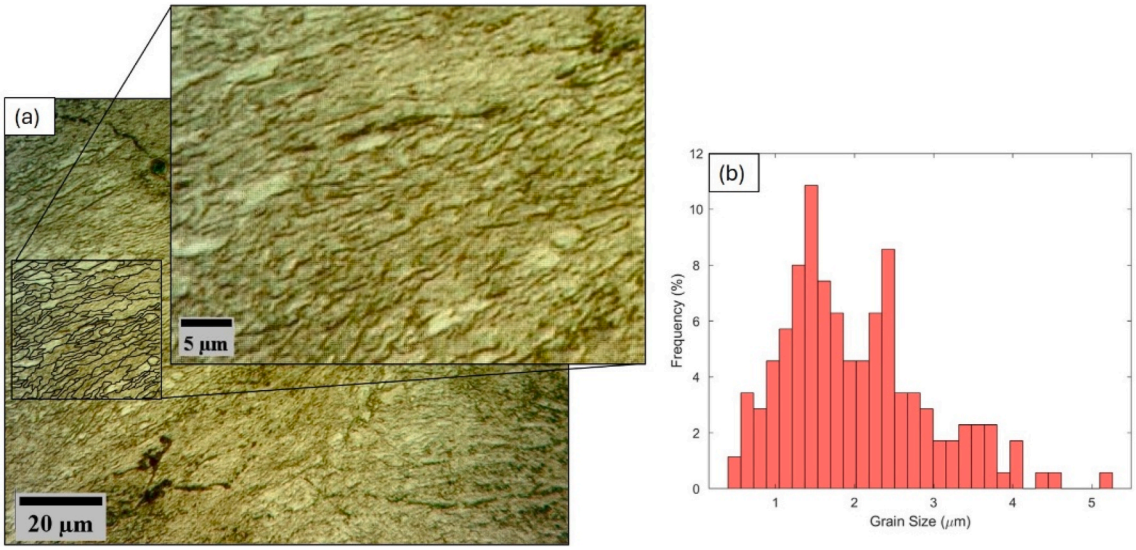

Fig. 3. (a) Magnified optical micrograph of the Mg–1Zn–0.2Ca alloy processed by 3 HPT turns at a radial distance of 6 mm, (b) Grain size frequency histogram corresponding to the microstructure in (a).

(Fig. 4a) and total effective strain (Fig. 4b) for different numbers of HPT turns, along with the as-cast condition for comparison. Fig. 4a shows that HPT processing leads to a pronounced increase in hardness compared to the as-cast alloy, which exhibits an average hardness of approximately 49.5 Hv and remains essentially constant across the disc radius. In contrast, all HPT-processed samples display significantly

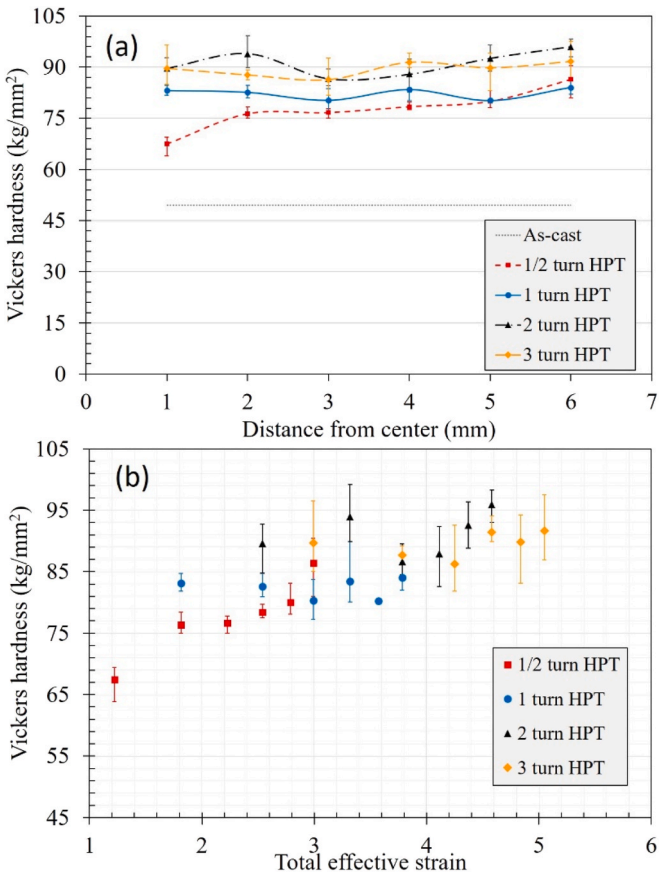

Fig. 4. Variation of Vickers hardness of the Mg–1Zn–0.2Ca alloy after HPT processing: (a) hardness as a function of distance from the disc center for different numbers of HPT turns, including the as-cast condition; (b) hardness as a function of total effective strain.

higher hardness values, with the hardness generally increasing with both the number of HPT turns and radial distance from the center. This trend reflects the non-uniform strain distribution inherent to the HPT process, where the imposed shear strain increases with increasing radius. At lower rotations (1/2 and 1 turn), a noticeable hardness gradient is observed, indicating incomplete microstructural homogenization. With increasing rotations (2 and 3 turns), the hardness distribution becomes more uniform, particularly at larger radial distances, suggesting the approach toward a saturation state in strain-induced strengthening.

Fig. 4b presents the hardness as a function of total effective strain, combining data from different radial positions and HPT turns. A clear positive correlation between hardness and effective strain is observed for all processing conditions. The hardness increases rapidly at lower strains and tends to level off at higher strains, indicating the onset of saturation in strengthening. This behavior is consistent with the evolution toward an ultrafine-grained structure and a high dislocation density with increasing strain. The highest hardness values, approaching 90–95 Hv, are achieved at the largest effective strains corresponding to higher HPT turns and outer disc regions. The hardness evolution shown in Fig. 4 confirms that the enhancement in mechanical properties of the Mg–1Zn–0.2Ca alloy is governed primarily by strain accumulation during HPT processing, which promotes grain refinement and defect strengthening, in agreement with the microstructural observations presented in Figs. 2 and 3.

3.3. Hardness evolution during Post-HPT annealing

Fig. 5 presents the variation in Vickers hardness and the corresponding optical microstructures of the HPT-processed Mg–1Zn–0.2Ca alloy during annealing at 300 (5a), 325 (5b), 350 (5c), 375 (5d), and 400 °C (5e) for different holding times. At all investigated temperatures, the hardness exhibits a non-monotonic dependence on annealing time, characterized by an initial decrease followed by a partial increase at longer holding times. At 300 °C (Fig. 5a), the hardness shows relatively small fluctuations with annealing time and remains at a comparatively high level throughout the investigated duration. The hardness evolution at 300 °C initially presents a subtle 'decrease-increase-decrease' pattern; however, the substantial overlap of error bars between the 200 s and 300 s intervals suggests these fluctuations remain within the margin of experimental scatter and do not represent a statistically significant deviation. At 325 °C (Fig. 5b), a more pronounced hardness variation is observed, with a clear minimum at intermediate annealing times followed by a noticeable increase at longer times. At 350 °C (Fig. 5c), a similar non-monotonic trend is observed; the hardness decreases significantly at intermediate times and subsequently increases at longer annealing times, although the minimum hardness is lower than that at 325 °C. At higher temperatures of 375 °C and 400 °C (Fig. 5d and e), the hardness decreases more rapidly with annealing time, reaching lower minimum values, and shows a partial recovery at prolonged holding times.

The corresponding optical micrographs in Fig. 5 reveal progressive microstructural evolution with increasing annealing time at all temperatures. At shorter annealing times, the microstructure retains features associated with the severely deformed UFG state. With increasing annealing time, the microstructure becomes more homogeneous and grain boundaries become more clearly defined. The extent and rate of microstructural evolution increase with annealing temperature, with more pronounced structural changes observed at 375 and 400 °C compared to 300, 325, and 350 °C. Fig. 5 demonstrates that both annealing temperature and holding time significantly influence the hardness response and microstructural development of the HPT-processed Mg–1Zn–0.2Ca alloy. To ensure a clear characterization of the hardening mechanism, 325 °C was selected as the representative temperature for detailed microstructural analysis. This temperature provides a stable and well-defined manifestation of the secondary hardening peak within the investigated time frame, effectively balancing the relatively sluggish kinetics of the 300 °C condition with the rapid microstructural evolution observed at 400 °C.

Fig. 6 presents a detailed microstructural characterization of the HPT-processed Mg–1Zn–0.2Ca alloy annealed at 325 °C for different holding times, based on quantitative analysis of optical microscopy images. The figure combines representative optical micrographs, corresponding grain size frequency histogram, and grain size distribution maps obtained through image-based grain boundary tracing in accordance with the ASTM E1382 standard. For the sample annealed for 150 s (Fig. 6a2), the grain size frequency histogram is relatively narrow and unimodal, with the majority of grains concentrated between approximately 1 and 2 μm and a limited fraction of grains larger than ~3 μm. This indicates a predominantly fine-grained microstructure with moderate grain size dispersion. After annealing for 200 s (Fig. 6b2), the grain size frequency histogram becomes noticeably broader and more asymmetric. While a significant fraction of grains remains in the fine-grained range, the distribution develops a pronounced tail extending toward larger grain sizes, reaching up to approximately 6–7 μm. This reflects an increase in grain size heterogeneity at this annealing time.

At an annealing time of 250 s (Fig. 6c2), the grain size frequency histogram becomes narrower again compared to the 200 s condition. The majority of grains are concentrated around 1–2 μm, and the fraction of coarse grains is reduced, indicating a more uniform grain size distribution across the analyzed area. With further annealing to 300 s (Fig. 6d2), the grain size frequency histogram shows no significant change, and the majority of grains remain within the UFG regime. The grain size frequency distributions reveal a non-monotonic evolution of grain size dispersion with annealing time at 325 °C, characterized by

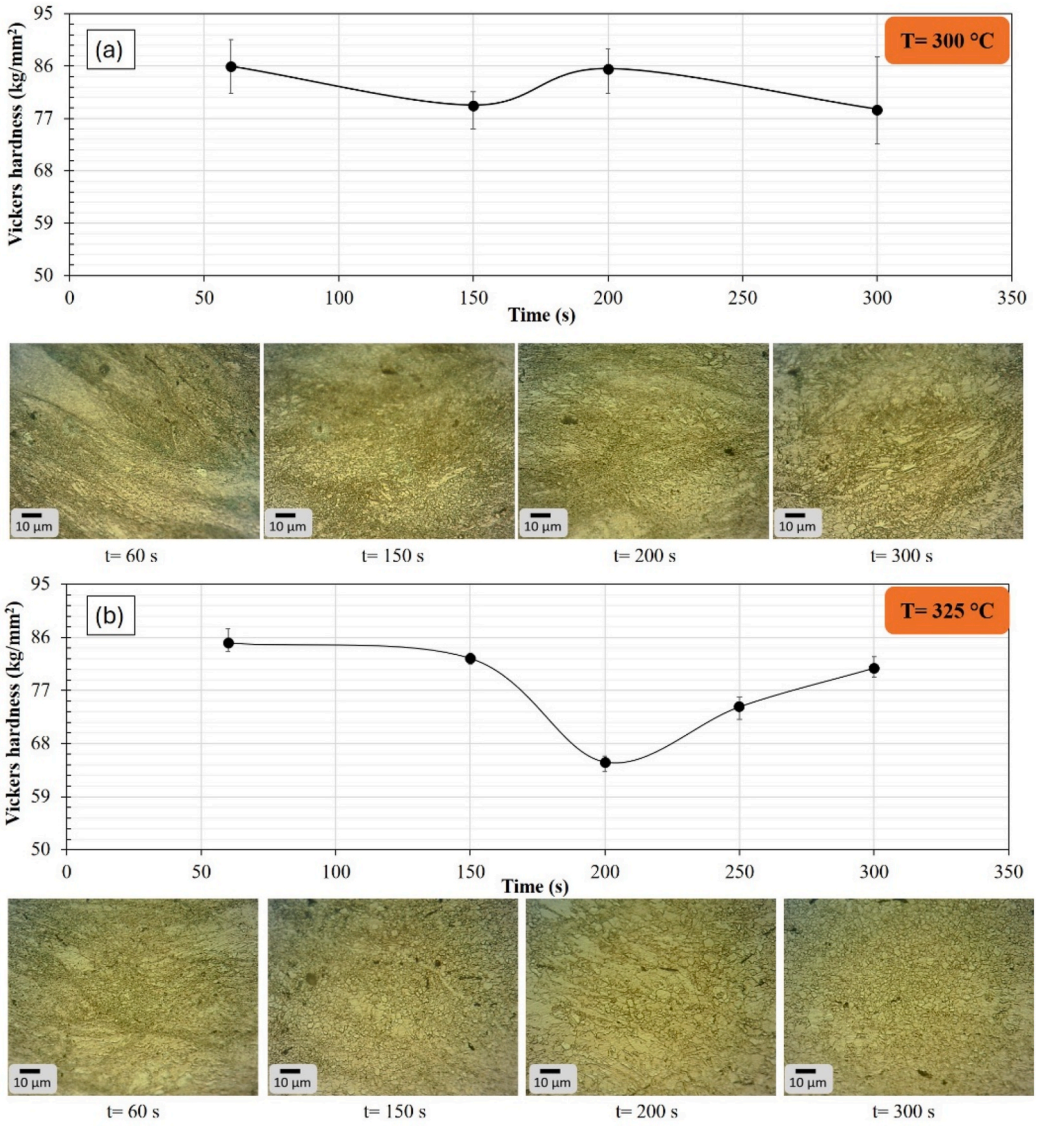

Fig. 5. Variation of Vickers hardness and corresponding optical microstructures of the HPT-processed Mg–1Zn–0.2Ca alloy during annealing at different temperatures: (a) 300 °C, (b) 325 °C, (c) 350 °C, (d) 375 °C and (e) 400 °C. Hardness is shown as a function of annealing time, with optical micrographs taken at selected holding times to illustrate the evolution of the microstructure.

alternating stages of broadening and narrowing of the distributions. These quantitative observations provide important input for the subsequent EBSD-based analysis of the microstructural state.

3.4. EBSD analysis of microstructural evolution

Fig. 7 presents EBSD inverse pole figure (IPF), grain orientation spread (GOS), and kernel average misorientation (KAM) maps of the HPT-processed Mg–1Zn–0.2Ca alloy annealed at 325 °C for 200, 250, and 300 s, providing quantitative insight into the evolution of crystallographic orientation, intragranular misorientation, and local lattice strain. For the sample annealed for 200 s (Fig. 7a1–a3), the IPF map reveals a fine-grained microstructure with a broad distribution of crystallographic orientations and no pronounced texture. The corresponding GOS map shows that the majority of grains exhibit very low GOS values, with approximately 90.4% of grains having GOS $\leq 1°$, while only a small fraction displays higher GOS values. Similarly, the KAM map indicates that about 93.0% of the area exhibits KAM $\leq 1°$, with limited regions showing higher local misorientation. These results indicate a microstructure that is largely strain-relieved but still contains isolated regions of residual intragranular misorientation.

After annealing for 250 s (Fig. 7b1–b3), the IPF map continues to show a fine-grained structure with increased grain size heterogeneity. The GOS distribution remains dominated by low values; however, the fraction of grains with GOS $>1°$ increases slightly compared to the 200 s condition. Correspondingly, the KAM map shows a modest increase in the fraction of regions with KAM $>1°$, indicating a higher degree of local lattice misorientation and strain heterogeneity at this annealing time, although low-KAM regions still dominate the microstructure. With further annealing to 300 s (Fig. 7c1–c3), the IPF map shows a more uniform and equiaxed grain structure. The GOS map indicates a further increase in the fraction of grains with very low GOS values, with approximately 93.9% of grains exhibiting GOS $\leq 1°$, suggesting a reduction in intragranular misorientation. Consistently, the KAM map is strongly dominated by low misorientation values, with approximately 97.1% of the area exhibiting KAM $\leq 1°$, indicating a more homogeneous and strain-relieved microstructural state.

The EBSD results demonstrate a subtle but non-monotonic evolution

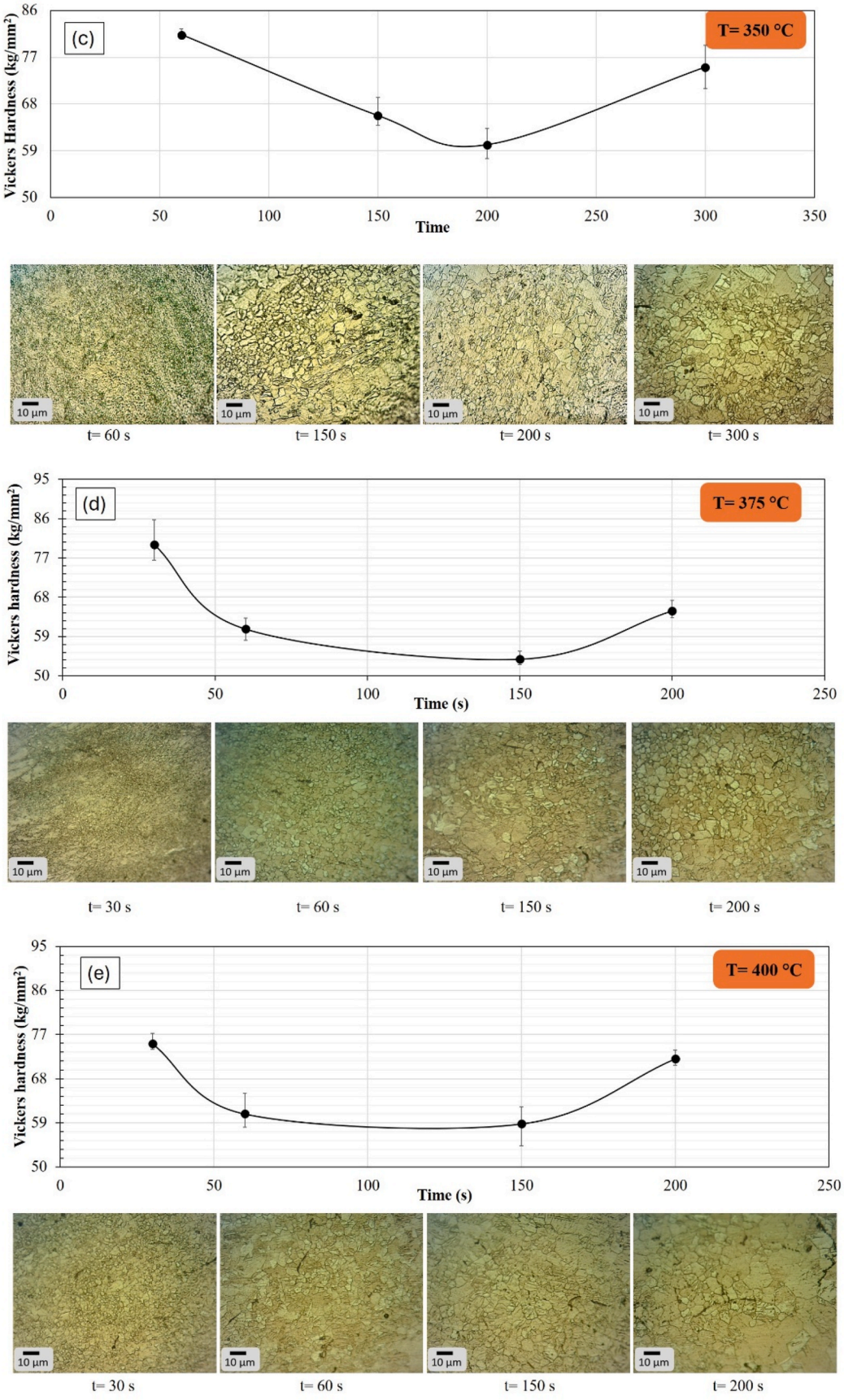

Fig. 5. (*continued*).

of intragranular misorientation and local lattice strain with annealing time at 325 °C. While low-GOS and low-KAM regions dominate at all

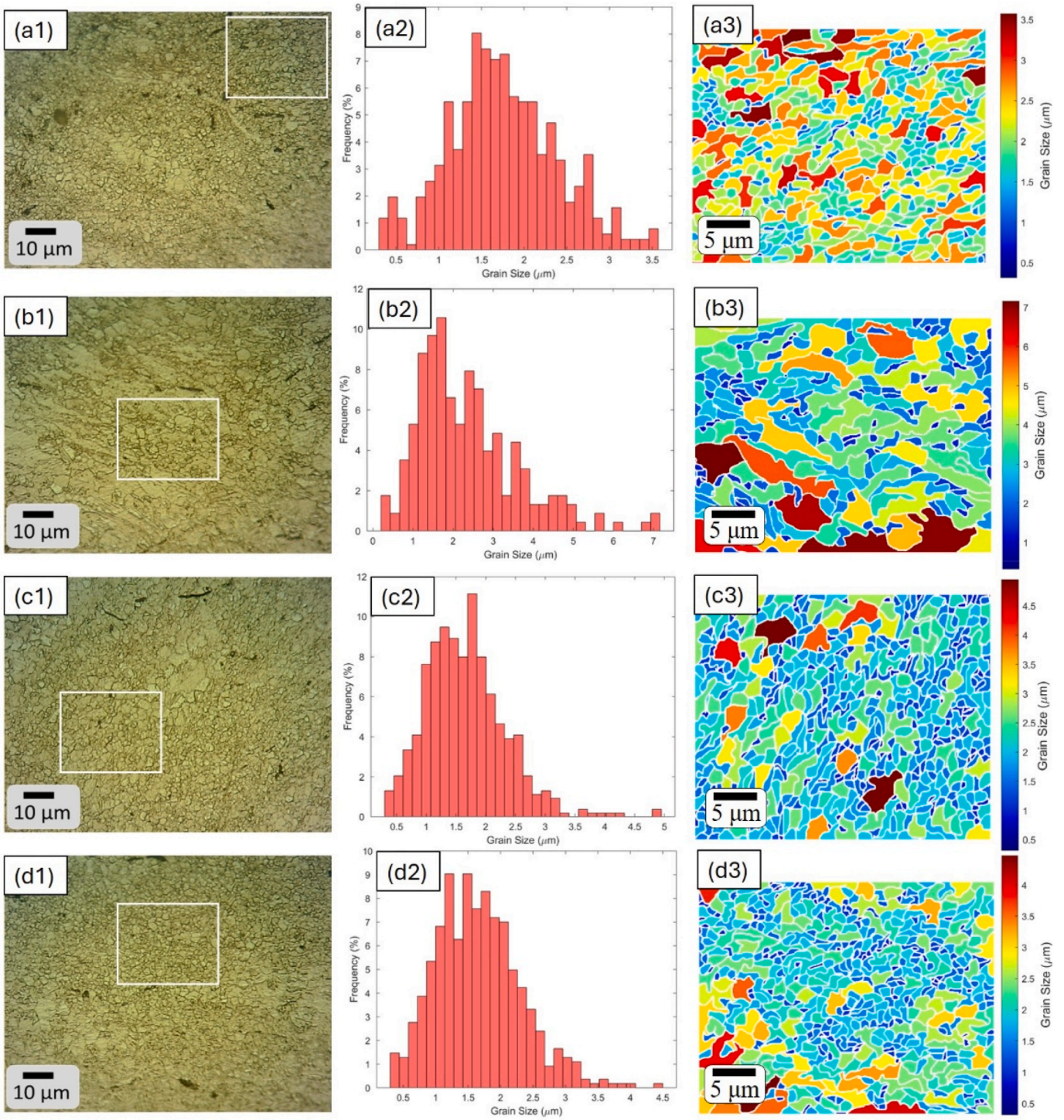

Fig. 6. Detailed microstructural analysis of the HPT-processed Mg–1Zn–0.2Ca alloy annealed at 325 °C for different holding times: (a) 150 s, (b) 200 s, (c) 250 s, and (d) 300 s. For each condition, (1) optical micrograph, (2) grain size frequency histogram obtained from image analysis following ASTM E1382, and (3) corresponding grain size distribution map generated by traced grain boundaries.

annealing times, a relative increase in misorientation heterogeneity is observed at 250 s, followed by a more uniformly strain-relieved microstructure at 300 s. These EBSD observations provide a quantitative basis for interpreting the anomalous hardness evolution observed during annealing at this temperature.

Fig. 7 presents overall the EBSD analysis of the samples annealed at 325 °C for 200 s and 250 s, indicating a fine-grained microstructure with generally low intragranular misorientation. To further examine the local microstructural characteristics underlying these observations, Figs. 8 and 9 provide a more detailed EBSD analysis of selected regions from the samples annealed for 200 s and 250 s, respectively. For the sample annealed for 200 s (Fig. 8), the high-magnification IPF maps confirm a refined and equiaxed grain structure with a random orientation distribution. The corresponding GOS maps show that a large majority of the grains exhibit low orientation spread, with approximately 90.5% of the grains having GOS values below 2°, indicating that most grains are in a relatively well-recovered state. The KAM maps further support this observation, as most of the scanned area exhibits KAM values below 2°,

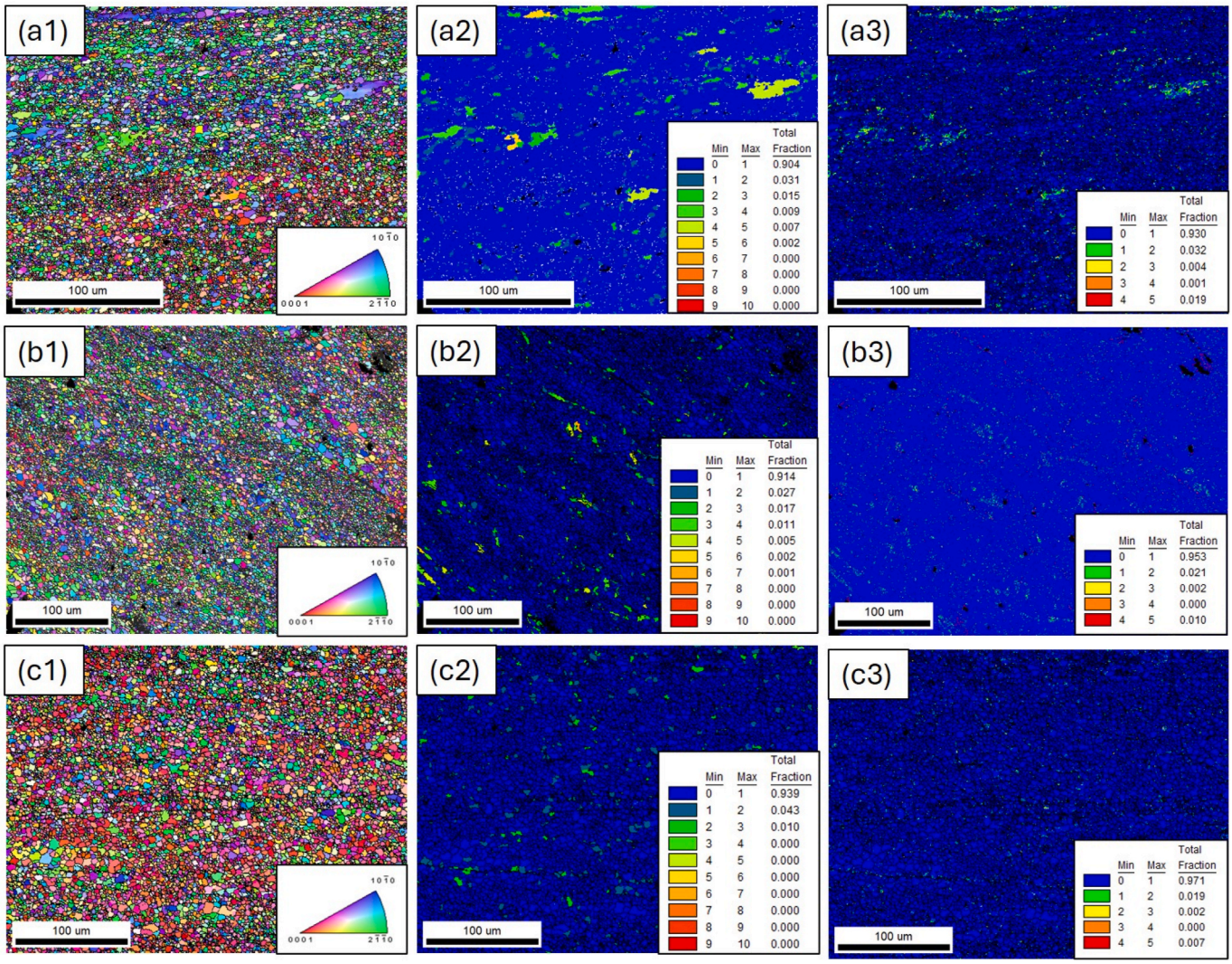

Fig. 7. EBSD characterization of the HPT-processed Mg–1Zn–0.2Ca alloy annealed at 325 °C for different holding times: (a) 200 s, (b) 250 s, and (c) 300 s. For each condition, IPF maps (1), grain GOS maps (2), and KAM maps (3) are shown.

reflecting a generally low level of local lattice misorientation, with only limited regions showing higher local strain.

In the case of the sample annealed for 250 s (Fig. 9), the IPF maps again reveal a fine-grained and equiaxed microstructure with improved spatial uniformity. The GOS maps indicate that the fraction of grains with GOS values below 2° decreases to approximately 77.4%, suggesting a more heterogeneous distribution of intragranular misorientation compared to the 200 s condition. Nevertheless, the KAM maps show that the majority of the analyzed area still exhibits KAM values below 2°, indicating that low local misorientation remains dominant despite the increased heterogeneity observed in the GOS distribution. A comparison between Figs. 8 and 9 demonstrates that, although both annealing conditions are characterized by predominantly low-misorientation microstructures, the distribution of intragranular misorientation becomes more heterogeneous at 250 s, as reflected by the reduced fraction of grains with GOS below 2°. These detailed EBSD observations are consistent with the large-area trends presented in Fig. 7 and provide important insight into the evolving microstructural state at intermediate annealing times.

Fig. 10 presents the statistical analysis of grain size distribution and grain boundary misorientation angle distribution for the samples annealed at 325 °C for 200 s, 250 s, and 300 s, corresponding to Fig. 10a, b, and 10c, respectively. For the sample annealed for 200 s (Fig. 10a1), the grain size distribution is dominated by fine grains, with the majority of grains smaller than 2 μm and an average grain size of approximately 1.62 μm. The distribution is right-skewed, with a small fraction of larger grains extending toward higher grain sizes. The corresponding misorientation angle distribution (Fig. 10a2) shows a broad range of misorientation angles, with a high fraction of high-angle grain boundaries, indicating a largely recrystallized or recovered grain structure.

After annealing for 250 s (Fig. 10b1), the grain size distribution shifts slightly toward larger sizes, and the average grain size increases to approximately 1.82 μm. Although fine grains still dominate the microstructure, the frequency of larger grains increases, indicating ongoing grain growth. The misorientation angle distribution (Fig. 10b2) remains broad and is similar to that of the 200 s condition, with high-angle grain boundaries continuing to dominate. For the sample annealed for 300 s (Fig. 10c1), a further shift toward larger grain sizes is observed, with the average grain size increasing to approximately 1.97 μm. The grain size distribution becomes slightly broader, reflecting continued grain growth with increasing annealing time. The corresponding misorientation angle distribution (Fig. 10c2) again shows a predominance of high-angle grain boundaries, with no substantial change in the overall shape of the distribution compared to shorter annealing times. The statistical analysis demonstrates a gradual increase in average grain size with increasing annealing time, while the misorientation angle distributions remain largely similar for all conditions, indicating that annealing primarily affects grain growth rather than significantly altering the grain

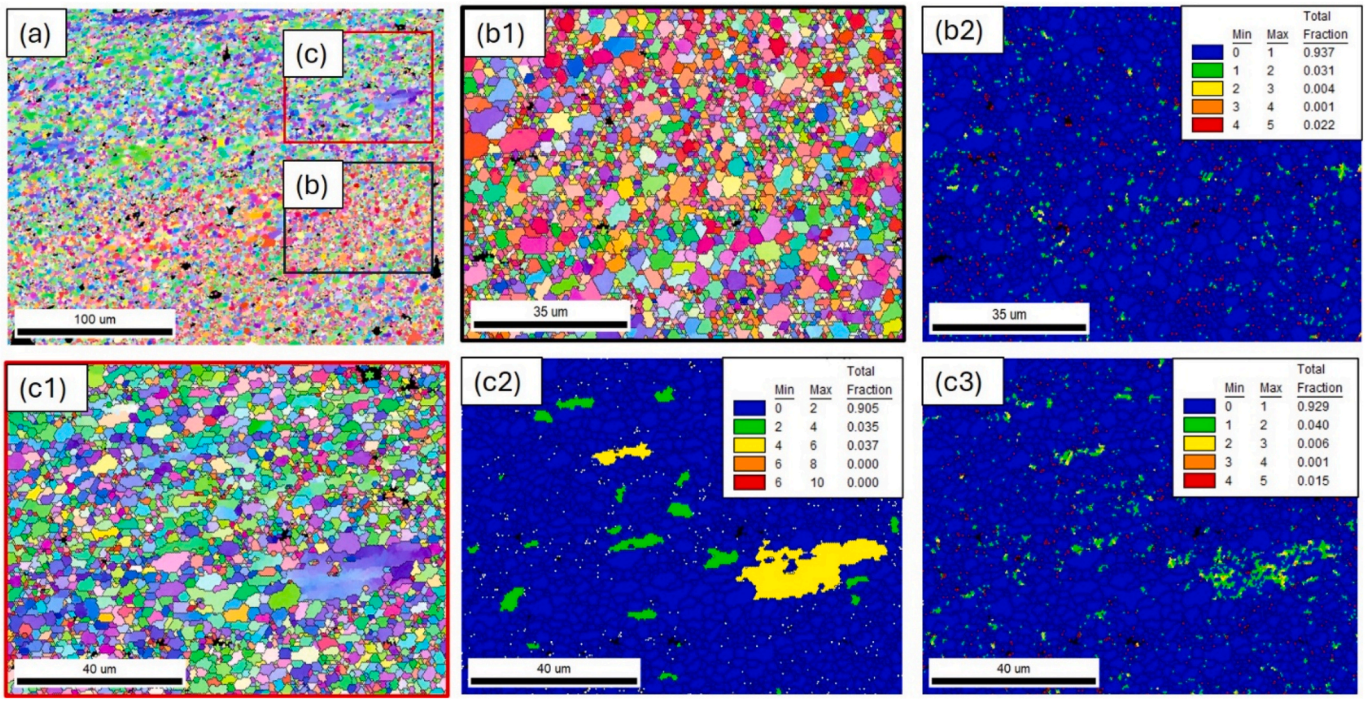

Fig. 8. Detailed EBSD analysis of the Mg–1Zn–0.2Ca alloy annealed at 325 °C for 200 s. (a) IPF map showing selected regions for local analysis. (b1) Enlarged IPF map of region b with the corresponding KAM map (b2). (c1) Enlarged IPF map of region c with the corresponding GOS map (c2) and KAM map (c3), illustrating local variations in grain orientation and intragranular misorientation.

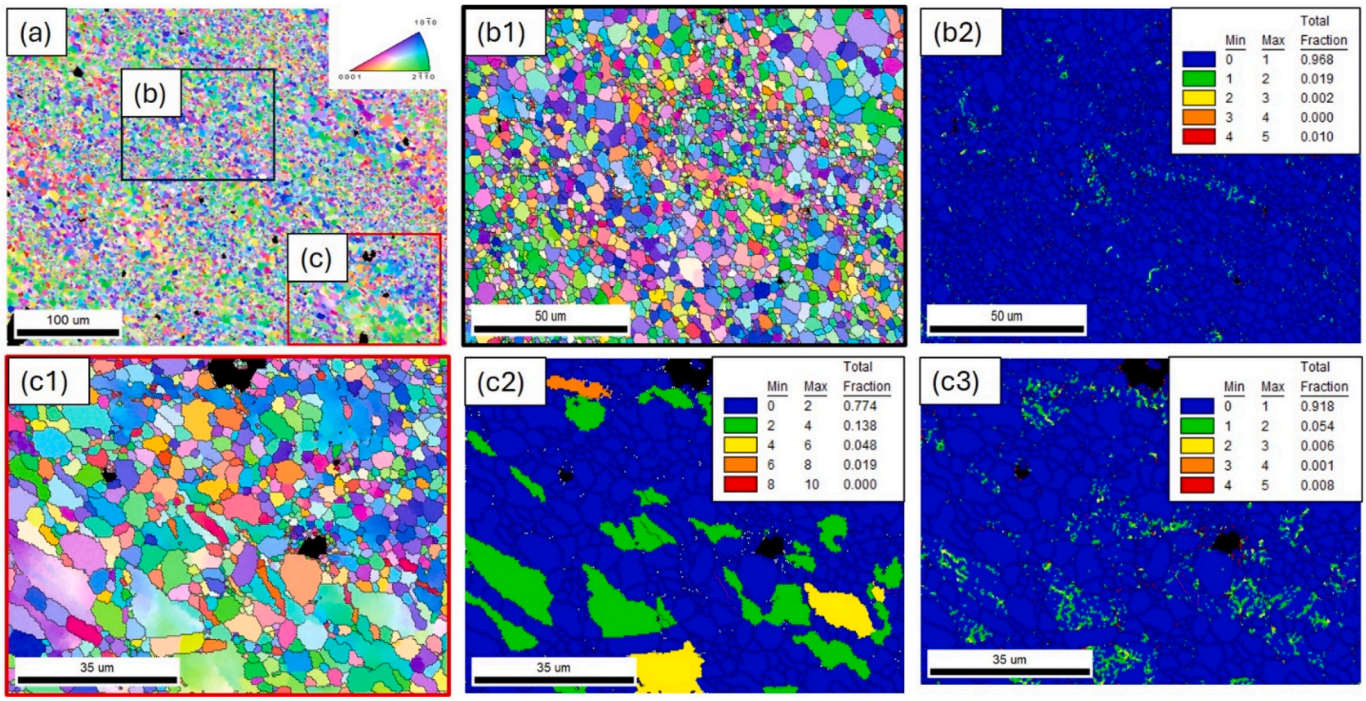

Fig. 9. Detailed EBSD analysis of the Mg–1Zn–0.2Ca alloy annealed at 325 °C for 250 s. (a) IPF map showing selected regions for local analysis. (b1) Enlarged IPF map of region b with the corresponding KAM map (b2). (c1) Enlarged IPF map of region c with the corresponding GOS map (c2) and KAM map (c3), illustrating local variations in grain orientation and intragranular misorientation.

boundary character distribution.

Fig. 11 presents the pole figures of the Mg–1Zn–0.2Ca alloy annealed at 325 °C for 200 s, 250 s, and 300 s, showing the orientation distribution of the (0001), (10 $\bar{1}$ 0), and (11$\bar{2}$ 0) planes. For the samples annealed for 200 s and 250 s (Fig. 11a and b), the overall shape and distribution of the pole figures remain largely similar for all three pole figures, indicating that the general texture components are preserved during annealing up to 250 s. In particular, no significant redistribution of orientation density is observed for the (10 $\bar{1}$ 0), and (11$\bar{2}$ 0) poles. However, a noticeable reduction in the maximum pole intensity is

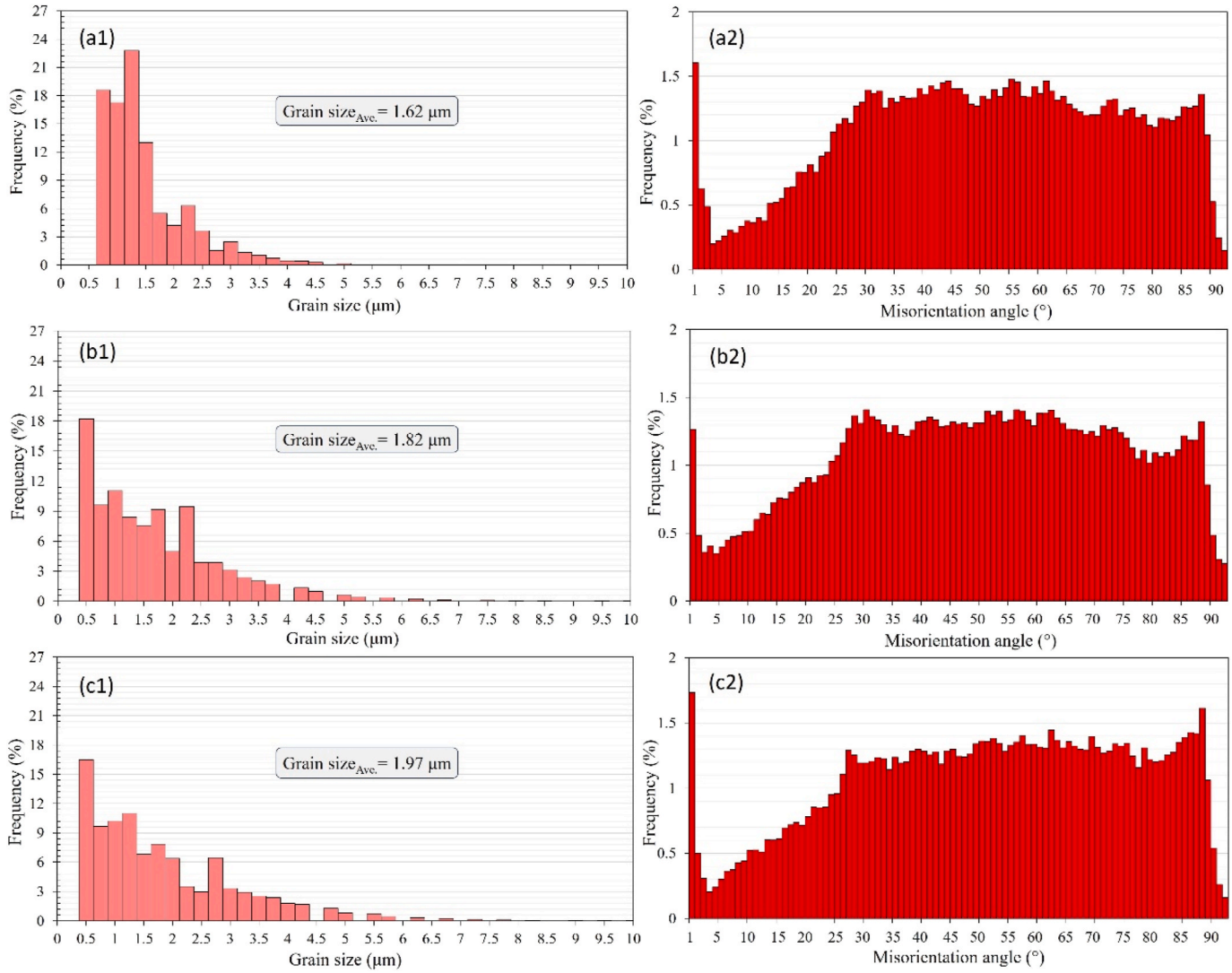

Fig. 10. Statistical analysis of grain size distribution (1) and grain boundary misorientation angle distribution (2) for the Mg–1Zn–0.2Ca alloy annealed at 325 °C for (a) 200 s, (b) 250 s, and (c) 300 s.

observed in the (0001) pole figure at 250 s, suggesting a weakening of basal texture intensity without a fundamental change in texture type.

After annealing for 300 s (Fig. 11c), discernible changes are observed in the pole figures for all three planes. The orientation density becomes more redistributed, and the intensity patterns differ from those observed at shorter annealing times. These changes indicate a modification of the overall texture state after prolonged annealing, reflecting further microstructural evolution beyond simple texture weakening. The pole figure analysis demonstrates that annealing at 325 °C up to 250 s primarily leads to a reduction in texture intensity—particularly for the (0001) pole—while preserving the general texture characteristics, whereas longer annealing times (300 s) result in a more pronounced change in the crystallographic orientation distribution.

4. Discussion

The hardness evolution of the HPT-processed Mg–1Zn–0.2Ca alloy during annealing exhibits a non-monotonic trend that cannot be explained solely by conventional annealing arguments. Although annealing generally promotes recovery, recrystallization and grain growth, leading to softening, an abnormal increase in hardness is observed at intermediate and longer annealing times. This behavior can be rationalized by considering the combined effects of heterogeneous recovery rate and crystallographic orientation–dependent deformation behavior. EBSD analysis reveals that annealing for 250 s results in a heterogeneous recovery rate, characterized by the coexistence of well-recovered grains and grains retaining higher intragranular misorientation. While KAM remains low over most of the microstructure, the reduced fraction of grains with low GOS indicates that recovery is not spatially uniform. During indentation, this heterogeneity leads to strain partitioning between regions with different recovery states, generating back-stress and additional constraint at grain boundaries. This constraint-controlled deformation increases the apparent resistance to indentation, giving rise to abnormal hardening despite the overall progress of recovery.

A notable feature of the EBSD analysis is the decrease in the fraction of grains with GOS $<2^{\circ}$ at 250 s, accompanied by an increase in the population of higher GOS values. At first glance, this behavior appears contradictory, since annealing is generally expected to promote recovery, reduce internal strain, and consequently increase the fraction of low-GOS grains. However, it is important to recognize that GOS reflects the average internal misorientation within each grain relative to its mean orientation, where low values ($<2^{\circ}$) indicate reduced internal lattice distortion and a more stabilized state, while higher values correspond to greater internal orientation gradients. The observed increase in higher GOS fractions at 250 s suggests that the microstructure

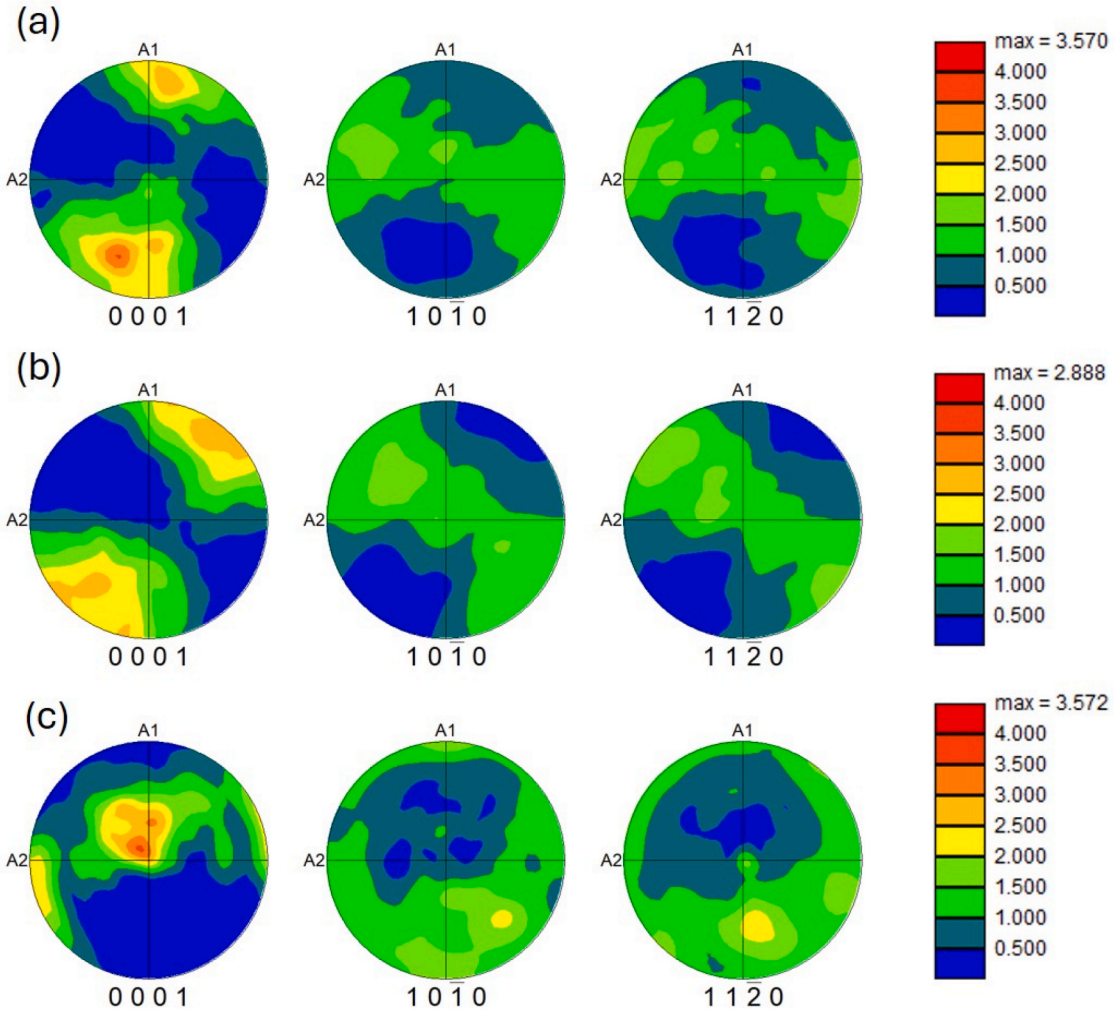

Fig. 11. Pole figures of the Mg–1Zn–0.2Ca alloy annealed at 325 °C for (a) 200 s, (b) 250 s, and (c) 300 s, showing the orientation distribution of the (0001), (10 $\bar{1}$ 0), and (11$\bar{2}$ 0) planes.

at this stage is not in a steady recovery regime but rather in a transitional state. During this intermediate stage, previously relaxed grains may undergo crystallographic reorientation, boundary migration, or subgrain rearrangement, processes that can temporarily increase internal orientation spread. In UFG HPT-processed materials, grain boundaries are highly strained and may become mobile during annealing, and their migration can induce local lattice rotations that are detected as elevated GOS values. Furthermore, the evolution of basal texture observed in the present study implies ongoing crystallographic adjustment, which can locally increase internal misorientation even while overall recovery progresses. Therefore, the decrease in low-GOS fraction at 250 s reflects spatially non-uniform and non-monotonic strain relaxation rather than a contradiction to annealing theory. The subsequent increase in low-GOS grains at longer annealing time (300 s) supports the interpretation that 250 s represents a transient microstructural adjustment stage prior to further stabilization.

The inverse pole figure maps and pole figure analysis indicate a concurrent evolution in crystallographic orientation. After 300 s, a large fraction of grains rotate such that the (0001) basal plane becomes preferentially aligned parallel to the observation surface, placing the indentation direction approximately perpendicular to the basal plane. Under this orientation condition, basal slip—normally the easiest deformation mode in magnesium—is geometrically unfavorable. As a result, plastic deformation during indentation must proceed predominantly through prismatic and pyramidal slip systems, which possess significantly higher critical resolved shear stresses than basal slip. The activation of these non-basal slip systems increases lattice friction and raises the effective flow stress required for deformation. Consequently, deformation accommodation becomes more difficult, leading to an increased resistance to indentation and a corresponding increase in hardness. This texture-induced hardening effect becomes increasingly pronounced at longer annealing times, after the initial softening associated with recovery has largely saturated. Therefore, the abnormal hardening observed during annealing arises from a synergistic interplay between heterogeneous recovery rate at intermediate annealing times and texture-controlled deformation mechanisms at longer annealing times. While recovery and recrystallization govern the initial softening behavior, the subsequent evolution of crystallographic orientation plays an important role in determining the post-annealing mechanical response. These results highlight the necessity of considering both microstructural heterogeneity and texture evolution when interpreting the mechanical behavior of severely deformed magnesium alloys subjected to annealing.

It should be noted that the texture intensity values reported in Fig. 11 correspond to the maximum values shown on the color scale rather than the exact peak intensity, and therefore should be interpreted qualitatively. The hardness evolution cannot be directly correlated with texture intensity alone. At intermediate annealing time (250 s), although the overall texture intensity decreases, EBSD analysis reveals increased heterogeneity in grain orientation spread, indicating non-uniform

recovery. This heterogeneous microstructural state promotes strain partitioning and back-stress strengthening during indentation, leading to an increase in hardness. With further annealing to 300 s, the microstructure becomes more uniformly recrystallized and heterogeneity is reduced. In this stage, texture evolution plays a more dominant role, where crystallographic reorientation—particularly the alignment of basal planes—modifies the deformation geometry and promotes the activation of harder non-basal slip systems. Therefore, the observed hardness evolution results from the interplay of heterogeneous recovery, recrystallization, and texture evolution, with their relative contributions changing as a function of annealing time.

As a summary, during annealing at 325 °C, the mechanical response is governed by the competition between softening mechanisms—namely recovery, recrystallization, and grain growth—and the hardening mechanisms identified in this study. The initial reduction in hardness is attributed to the combined effect of dislocation recovery within the deformed matrix and the nucleation of strain-free recrystallized grains, as evidenced by the decrease in KAM and GOS values. However, the subsequent secondary hardening indicates that the strengthening contribution from misorientation heterogeneity and crystallographic reorientation outweighs the softening effects of recrystallization and grain coarsening. This distinction is supported by the EBSD data, which shows that the hardening coincides with a significant weakening of the basal texture, even as the recrystallized area fraction continues to evolve.

The present hardening behavior can be interpreted within the broader framework of AH reported for HPT-processed materials, where defect reconfiguration and microstructural stabilization lead to an increase in hardness even after initial recovery. As reviewed by Gubicza [31], AH in fine-grained materials can arise from several defect- and boundary-related mechanisms, including grain boundary relaxation, annihilation of mobile dislocations, reduction in the density of easy dislocation sources, and the evolution of a hard crystallographic texture. Importantly, these strengthening effects occur even when grain size remains constant or increases slightly, indicating that defect reconfiguration rather than grain refinement governs the response.

Early investigations on HPT-processed ultrafine-grained Ni_3Al showed that annealing transformed non-equilibrium grain boundaries into more stable configurations, which correlated with an increase in hardness. This led to the concept of non-equilibrium grain boundary "transparency," whereas-deformed boundaries facilitate easier deformation while relaxed boundaries hinder dislocation transmission [32]. Similar conclusions were drawn in UFG Ni–Mo alloys, where hardening was attributed to the annihilation of mobile dislocations combined with the clustering of remaining dislocations into low-energy configurations. In these cases, annealing reduced the density of mobile defects while decreasing the availability of dislocation sources, resulting in higher resistance to plastic flow [33]. In Mg–Zn–Ca alloys specifically, Horky et al. [24] suggested that high vacancy concentrations from HPT can lead to the formation of vacancy agglomerates and dislocation loops during heat treatment, acting as strong obstacles to dislocation motion.

These studies collectively demonstrate that AH is a reproducible phenomenon across a wide range of materials. In nanostructured Cu–Al alloys, annealing promoted the formation of nanoscale twins due to high residual stresses, leading to enhanced strength [34]. Similarly, AH has been observed in high-entropy [35,36] and medium-entropy [37] alloys, where strengthening was attributed to dislocation rearrangement, grain boundary relaxation, or precipitation phenomena. Other systems show chemical contributions; for instance, in Al–Zn alloys [38], unusual hardening was linked to spinodal decomposition, and in Ti/Al_2O_3 nanocomposites [39], strengthening was attributed to the dissolution of alloying elements and formation of interfacial reaction products. Ultimately, the literature establishes that AH in HPT-processed materials is not anomalous but a characteristic response of highly defected UFG microstructures.

The literature establishes that AH in HPT-processed materials is not anomalous but rather a characteristic response of highly defected UFG microstructures. The dominant mechanisms generally involve defect annihilation accompanied by structural stabilization of grain boundaries, reduction of mobile dislocation sources, and in some cases solute redistribution or defect clustering, all of which increase the resistance to subsequent plastic deformation despite partial recovery. Taken together with the microstructural and texture analyses presented earlier, the present hardening behavior can therefore be interpreted within the broader framework of AH reported for HPT-processed materials, where defect reconfiguration and microstructural stabilization during annealing lead to an increase in hardness even after an initial recovery stage.

5. Conclusions

The present study systematically examined the microstructural evolution and hardness behavior of an Mg–1Zn–0.2Ca alloy processed by HPT and subsequently annealed at different temperatures and times. Particular emphasis was placed on clarifying the origin of the abnormal, non-monotonic hardness variation observed during post-deformation annealing.

1. The initial grain size of ~105 μm was refined to the ultrafine range through HPT processing and subsequent annealing (300–400 °C), yielding average grain sizes of 1.62–1.97 μm depending on annealing time. Subsequent annealing at 300–400 °C produced a non-monotonic hardness evolution characterized by an initial softening stage followed by a distinct hardness increase with increasing annealing time. This abnormal behavior was consistently observed across the investigated temperature range, indicating that the hardening phenomenon is intrinsic to the post-HPT microstructural evolution.
2. Quantitative optical microscopy analysis demonstrated progressive grain coarsening during annealing at all temperatures. Since the hardness increase occurred despite grain growth, the abnormal hardening cannot be attributed to grain refinement or conventional Hall–Petch strengthening, suggesting the operation of alternative strengthening mechanisms.
3. EBSD characterization revealed a reduction in KAM and GOS at intermediate annealing times, indicating heterogeneous recovery rate within the UFG microstructure. The redistribution of internal strain during this stage contributes to the initial softening and modifies the subsequent mechanical response.
4. With prolonged annealing, significant changes in crystallographic texture were observed, particularly a weakening of the basal texture intensity accompanied by crystallographic reorientation of grains. These textural modifications alter the deformation geometry under indentation and contribute to the increased resistance to plastic deformation.
5. The abnormal hardening during annealing is therefore governed by the combined influence of heterogeneous recovery rate and basal texture modification rather than grain refinement. The results demonstrate that controlled annealing after severe plastic deformation can substantially alter the mechanical response of UFG Mg alloys through microstructural and crystallographic evolution, providing insight into strength tailoring strategies for magnesium-based materials.

CRediT authorship contribution statement

N. Mirabdolazimi: Investigation, M. Reihanian: Writing original draft, Writing-review and editing. E. Bagherpour: Formal analysis. C.L. Mendis: Formal analysis. A. Rezvani: Formal analysis. R.Z. Valiev: Conceptualization. R. Ebrahimi: Supervision, Conceptualization, Methodology.

Declaration of competing interest

The authors declare that they have no known competing financial interests or personal relationships that could have appeared to influence the work reported in this paper.

Acknowledgment

This work is based upon research funded by Iran National Science Foundation (INSF) under project No.4021954 and Russian Science Foundation (RSF) under project No. 24-43-20015. EB and CLM would like to acknowledge the use of the BCAST Advanced Characterization Suite (BACS) set up through the funding received from UKRI Infrastructure grant: entitled “Future Metallurgy Centre”.

Data availability

The raw/processed data required to reproduce these findings can be shared upon request.

References

[1] Zhang T, Wang W, Liu J, Wang L, Tang Y, Wang K. A review on magnesium alloys for biomedical applications. Front Bioeng Biotechnol 2022;10:953344.
[2] Vinogradov A, Merson E, Myagkikh P, Linderov M, Brilevsky A, Merson D. Attaining high functional performance in biodegradable Mg-Alloys: an overview of challenges and prospects for the mg-zn-ca System. Materials 2023;16:1324.
[3] Istrate B, Munteanu C, Antoniac I-V, Lupescu Ş-C. Current research studies of mg–ca–zn biodegradable alloys used as orthopedic implants. Crystals 2022;12:1468.
[4] Mansoor P, Dasharath S. Microstructural and mechanical properties of magnesium alloy processed by severe plastic deformation (SPD)–a review. Mater Today Proc 2020;20:145–54.
[5] Vinogradov A, Serebryany VN, Dobatkin SV. Tailoring microstructure and properties of fine grained magnesium alloys by severe plastic deformation. Adv Eng Mater 2018;20:1700785.
[6] Bryła K, Horky J. Magnesium alloys processed by severe plastic deformation (SPD) for biomedical applications: an overview. Mater Trans 2023;64:1709–23.
[7] Yamashita A, Horita Z, Langdon TG. Improving the mechanical properties of magnesium and a magnesium alloy through severe plastic deformation. Mater Sci Eng, A 2001;300:142–7.
[8] Kim WJ, An CW, Kim YS, Hong SI. Mechanical properties and microstructures of an AZ61 Mg Alloy produced by equal channel angular pressing. Scr Mater 2002;47:39–44.
[9] Figueiredo RB, Langdon TG. Principles of grain refinement in magnesium alloys processed by equal-channel angular pressing. J Mater Sci 2009;44:4758–62.
[10] Zhilyaev AP, Langdon TG. Using high-pressure torsion for metal processing: fundamentals and applications. Prog Mater Sci 2008;53:893–979.
[11] Edalati K. Review on recent advancements in severe plastic deformation of oxides by high-pressure torsion (HPT). Adv Eng Mater 2019;21:1800272.
[12] Abdulov RZ, Valiev RZ, Krasilnikov NA. Formation of submicrometre-grained structure in magnesium alloy due to high plastic strains. J Mater Sci Lett 1990;9:1445–7.
[13] Valiev RZ, Krasilnikov N, Tsenev N. Plastic deformation of alloys with submicron-grained structure. Mater Sci Eng, A 1991;137:35–40.
[14] Zhang CZ, Zhu SJ, Wang LG, Guo RM, Yue GC, Guan SK. Microstructures and degradation mechanism in simulated body fluid of biomedical mg–zn–ca alloy processed by high pressure torsion. Mater Des 2016;96:54–62.
[15] Gao JH, Guan SK, Ren ZW, Sun YF, Zhu SJ, Wang B. Homogeneous corrosion of high pressure torsion treated mg–zn–ca alloy in simulated body fluid. Mater Lett 2011;65:691–3.
[16] Zhang C, Guan S, Wang L, Zhu S, Wang J, Guo R. Effect of solution pretreatment on homogeneity and corrosion resistance of biomedical mg–zn–ca alloy processed by high pressure torsion. Adv Eng Mater 2017;19:1600326.
[17] Guan S, Ren ZW, Gao JH, Sun YF, Zhu SJ, Wang LG. *In vitro* degradation of Ultrafine grained mg-zn-ca alloy by high-pressure torsion in simulated body fluid. Mater Sci Forum 2012;706–709:504–9.
[18] Medeiros MP, Carvalho AP, Isaac A, Afonso CRM, Janeček M, Minárik P, Celis MM, Figueiredo RB. Using high pressure torsion to process magnesium alloys for biological applications. J Mater Res Technol 2023;22:3075–84.
[19] Brunner P, Brumbauer F, Steyskal E-M, Renk O, Weinberg A-M, Schroettner H, Würschum R. Influence of high-pressure torsion deformation on the corrosion behaviour of a bioresorbable Mg-based alloy studied by positron annihilation. Biomater Sci 2021;9:4099–109.
[20] Kulyasova OB, Khudododova GD, Dyakonov GS, Zheng Y, Valiev RZ. Effect of microstructure refinement on the corrosion behavior of the bioresorbable Mg-1Zn-0.2 Ca and Mg-1Ca alloys. Materials 2022;15:6749.
[21] Zhang C, Guan S, Wang L, Zhu S, Chang L. The microstructure and corrosion resistance of biological mg–zn–ca alloy processed by high-pressure torsion and subsequently annealing. J Mater Res 2017;32:1061–72.
[22] Zhang C, Liang C, Liang T, Si X, Jiang C. Enhanced mechanical properties of an mg-zn-ca alloy via high pressure torsion and annealing for use in bone implantation. Materia 2022;27:e20220005.
[23] Kulyasova OB, Islamgaliev RK, Zhao Y, Valiev RZ. Enhancement of the mechanical properties of an mg–zn–ca alloy using high-pressure torsion. Adv Eng Mater 2015;17:1738–41.
[24] Horky J, Ghaffar A, Werbach K, Mingler B, Pogatscher S, Schäublin R, Setman D, Uggowitzer PJ, Löffler JF, Zehetbauer MJ. Exceptional strengthening of biodegradable mg-zn-ca alloys through high pressure torsion and subsequent heat treatment. Materials 2019;12:2460.
[25] Hadi S, Rahimzadeh Lotfabad F, Paydar M, Ebrahimi R. New mathematical stress analysis in the compressive stage of the high-pressure torsion process. Met Mater Int 2021;27:2947–56.
[26] Pardis N, Ebrahimi R, Kim HS. Equivalent strain at large shear deformation: theoretical, numerical and finite element analysis. J Appl Res Technol 2017;15:442–8.
[27] Ghajar AJ, Cengel D Yunus A. Heat and mass transfer: fundamentals and applications. McGraw-Hill Education; 2014.
[28] Zheng A, Wan K, Huang Y, Ma Y, Ding T, Zheng Y, Chen Z, Feng Q, Du Z. Constructing anisotropic conductive networks inside hollow elastic fiber with high sensitivity and wide-range linearity by cryo-spun drying strategy. Adv Fiber Mater 2024:1–12.
[29] Jiao C, Jiang L, Chen X, Yao Y, Chen J, Wang X, Wang H, Feng Q, Ye D. Cotton-based metafabrics with asymmetric wettability for breathable, antibacterial, and directional moisture management. Adv Compos Hybrid Mater 2026;9:173.
[30] Qin K, Zhang D, Ma B, Gao W, Cao C, Zhu X, Lu J, Wang W, Ge J, Feng Q. Hydrophobic high-frequency vibration collaborative strategy for reducing resistance and soil adhesion of tillage tools in lime concretion black soil. Soil Tillage Res 2026;258:107061.
[31] Gubicza J. Annealing-induced hardening in ultrafine-grained and nanocrystalline materials. Adv Eng Mater 2020;22:1900507.
[32] Languillaume J, Chmelik F, Kapelski G, Bordeaux F, Nazarov A, Canova G, Esling C, Valiev R, Baudelet B. Microstructures and hardness of ultrafine-grained Ni3Al. Acta Metall Mater 1993;41:2953–62.
[33] Gubicza J, Pereira PHR, Kapoor G, Huang Y, Vadlamani SS, Langdon TG. Annealing-Induced hardening in ultrafine-grained Ni–Mo alloys. Adv Eng Mater 2018;20:1800184.
[34] Tao J, Chen G, Jian W, Wang J, Zhu Y, Zhu X, Langdon TG. Anneal hardening of a nanostructured Cu–Al alloy processed by high-pressure torsion and rolling. Mater Sci Eng, A 2015;628:207–15.
[35] Tang Q, Huang Y, Huang Y, Liao X, Langdon T, Dai P. Hardening of an Al0.3CoCrFeNi high entropy alloy via high-pressure torsion and thermal annealing. Mater Lett 2015;151:126–9.
[36] Shahmir H, He J, Lu Z, Kawasaki M, Langdon TG. Effect of annealing on mechanical properties of a nanocrystalline CoCrFeNiMn high-entropy alloy processed by high-pressure torsion. Mater Sci Eng, A 2016;676:294–303.
[37] Praveen S, Bae JW, Asghari-Rad P, Park JM, Kim HS. Annealing-induced hardening in high-pressure torsion processed CoCrNi medium entropy alloy. Mater Sci Eng, A 2018;734:338–40.
[38] Alhamidi A, Edalati K, Horita Z, Hirosawa S, Matsuda K, Terada D. Softening by severe plastic deformation and hardening by annealing of aluminum–zinc alloy: significance of elemental and spinodal decompositions. Mater Sci Eng, A 2014;610:17–27.
[39] Shahmir H, Langdon TG. Using heat treatments, high-pressure torsion and post-deformation annealing to optimize the properties of Ti-6Al-4V alloys. Acta Mater 2017;141:419–26.